THESIS FOR THE DEGREE OF DOCTOR OF PHILOSOPHY

Ion Solvation in Critical Binary Aqueous Solvents Probed by Advanced Synchrotron-Based Techniques

Monika Witala

UNIVERSITY OF GOTHENBURG

Department of Chemistry and Molecular Biology

2016

ISBN 978-91-628-9845-8 (print)
ISBN 978-91-628-9844-1 (PDF)
Available online at: http://hdl.handle.net/2077/43217

Printed by INEKO
Gothenburg, Sweden 2016

List of Papers

Paper I **Microscopic segregation of hydrophilic ions in critical binary aqueous solvents**
M. Witala, R. Nervo, O. Konovalov and K. Nygård
Soft Matter
11, 5883-5888 (2015)

Paper II **Relative adsorption excess of ions in binary solvents determined by grazing-incidence x-ray fluorescence**
M. Witala and K. Nygård
Manuscript

Paper III **Mesoscale ordering in binary aqueous solvents induced by ion size asymmetry**
M. Witala, S. Lages and K. Nygård
Soft Matter
In press, DOI: 10.1039/C6SM00580B (2016)

Paper IV **In situ small-angle x-ray scattering characterization of x-ray-induced local heating**
M. Witala, J. Han, A. Menzel and K. Nygård
J. Appl. Cryst.
47, 2078-2080 (2014)

Contribution report

`All papers`
In this thesis work, I planned, prepared and carried out all experiments and took an active role in the interpretation of the results.

`Paper I - II`
I wrote the successful experiment proposal, analyzed the data using self-written MATLAB® scripts and wrote the paper.

`Paper III`
I analyzed the data with self-written MATLAB® scripts and wrote the paper.

`Paper IV`
I was a contributing author.

Most common abbreviations

`2,6-DMP`	2,6-dimethylpyridine (2,6-lutidine)
`C2 ... C7`	tetra-n-alkylammonium bromides (from Et_4NBr up to Hep_4NBr)
`GIXF`	grazing-incidence x-ray fluorescence
`SAXS`	small-angle x-ray scattering

Contents

1 Introduction

In this first introductory chapter, I will give the underlaying motivation to my research studies, which resulted in the published articles.

1.1 Background

Since many years, the standard tool for studying electrostatic interactions in electrolyte solutions is the Poisson-Boltzmann approximation. However, this approximation neglects the size of the ions and ion-ion correlations, which seems to be important in real systems, e.g. including multivalent counterions [1]. The aforementioned approximation cannot explain the experimentally observed ion specific effects [2, 3]. Some investigations of electrolyte solutions at liquid-air [4] and liquid-liquid interface [5] indicated the ion-solvent coupling as responsible for the observed ion specificity.

The importance of ion-solvent coupling becomes even more evident in the case of binary mixed solvents. Adding ions to the critical binary solvents leads to range of fascinating phenomena. For instance, adding a simple inorganic salt may give rise to anomalous interactions between colloidal particles suspended in critical aqueous binary mixtures [6, 7]. On the other hand, the presence of the so-called antagonistic salt causes a weak assembly behavior in such mixtures [8, 9]. The antagonistic salt can be simply understood as a salt built of inorganic and organic ions, e.g. sodium tetraphenylborate ($NaBPh_4$). The case with antagonistic salt is also in contrast to the behavior of mixtures with simple salts, where the latter do not induce the mesoscale ordering. Lately, the antagonistic salt has been applied to stabilize a colloidal suspension [10].

1.2 Electrostatics in binary solvents

Let's imagine the binary liquid mixture containing immersed colloidal particles upon approaching the critical point of solvent's demixing. Due to confinement of diverging concentration fluctuations, an effective force arises between solid surfaces. This force, the critical Casimir force, has been observed indirectly through the thickness of wetting films [11] and later used in studies of capillary bridge formation in binary mixtures [12]. Already some years prior to direct measurements of critical Casimir forces [13], a reversible aggregation of polystyrene spheres in binary solvent at its critical composition has been noticed [14]. This critical Casimir

force [7, 13, 15] is strongly temperature-dependent, since its spatial extent is determined by the diverging bulk correlation length $\xi(T)$ of the mixture's critical fluctuations. As a consequence, critical Casimir forces are being applied e.g. for reversible control of colloidal aggregation [16, 17] or in precise control of the aggregates morphology [18] using temperature as a tuning parameter. While these critical forces are well understood in neat binary solvents, this is not the case upon the addition of salt. In the presence of hydrophilic salt these forces have been observed to appear several degrees farther from the critical point [6]. Moreover, the coupling between critical fluctuations and ion distributions in binary solvents has been found to induce an attraction between suspended hydrophilic and hydrophobic surfaces, despite the electrical double layer and critical Casimir forces are expected to be mutually repulsive. For the successful application of critical Casimir forces in colloidal systems, the surprising behavior in the presence of simple ions must be understood. A possible explanation is given by an unequal partitioning of hydrophilic ions due to their asymmetric solvation preferences [19–22]. Accordingly, the cations would accumulate near the suspended hydrophobic surface, driven by their weaker hydrophilicity compared to the anions [23]. However, the above mentioned unequal partitioning of hydrophilic ions has not yet been observed directly in an experiment.

The case of the antagonistic salt inducing mesoscale ordering, brought a significant interest within soft matter field [8, 9, 24]. Even a small concentration of these types of salts leads to emergence of structuring in the sample, which evolves in a salt content-dependent manner [8, 25, 26]. Initially, the underlaying mechanism was attributed to the ion partitioning based on hydrophilicity or hydrophobicity of cations and anions respectively. The antagonistic salt would behave as a surfactant [27, 28]. However, the aforementioned interpretation is still under debate. A theoretical model with equal-sized ions does not show the effect of mesoscale ordering [20] and an alternative prediction suggests the asymmetry of the ions' size as the governing mechanism [29]. Unfortunately, no system has been available for experimental verification. Previous experiments were conducted on systems exhibiting always a significant size asymmetry between the ions [8, 24, 26, 30].

1.3 Aim of this thesis work

In order to address the aforementioned phenomena in binary aqueous solvents containing either simple inorganic salt or antagonistic salt I make use of advanced synchrotron-based techniques. First, I probed the distribution of hydrophilic ions at the liquid-vapor interface of a critical binary mixture by using grazing-incidence x-ray fluorescence (GIXF). The main objective in this study (paper **I**) was to verify the theoretically suggested preferential solvation of hydrophilic ions, in a direct measurement. Further developing this idea, the goal was to quantify the unequal ion partitioning (paper **II**). For this purpose, I propose a method for determining ion relative surface excess at the binary liquid-vapor interface. I follow the previous idea [4] of binding the GIXF intensity with the surface excess Γ. Second, by choosing a new experimental system I performed small-angle x-ray scattering (SAXS) measurements to investigate the ion size asymmetry as a possible leading factor to the mesoscale ordering of the binary solvent (paper **III**). Such a new system had to be built of salt series with evolving cation-to-anion size ratio, allowing for systematic study of the ion size asymmetry effects. Additionally, I demonstrate the application of my critical binary liquid mixture as a system to

determine the x-ray beam-induced heating up of a liquid sample in a standard glass capillary (paper **IV**).

This thesis work will contribute to the clarification of the salt-induced effects in critical aqueous binary solvents.

In the following chapters I will describe: the experimental systems, used techniques, summarize the results and give future outlook. The four articles contributing to this work are included at the end (papers ***I*** *–* ***IV****).*

2 Experimental system

In this thesis work the studied system was a binary critical mixture containing salt. Here, I will describe the part of the work done in laboratory in order to verify the effects of added ions on the mixture's phase behavior.

2.1 Water and 2,6-dimethylpyridine mixture

A binary liquid mixture is a two-component system prepared by mixing two liquids. Some binary mixtures are miscible only under certain conditions and become phase separated when e.g. temperature is changed. Indeed, this is the case of the binary solvent used in this study. This mixture is fully miscible at room temperature, although heating causes reaching the lower critical point after which the two separated liquid phases are observed. Further increase of the temperature eventually results in reaching the upper critical point, after which the system becomes miscible again [15]. A schematic phase diagram for binary liquid mixture with a lower critical temperature is shown in Fig. 2.1. My experimental liquid mixture exhibits both critical points, however I only worked close to the lower T_C.

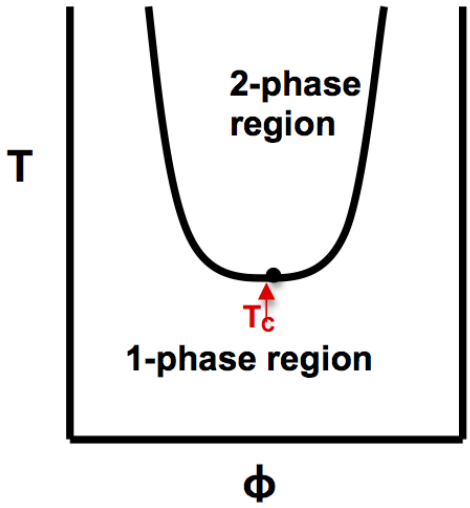

Figure 2.1: A schematic representation of the phase diagram of a binary liquid mixture, with a focus on a lower critical point (marked T_C as red). The phase behavior is presented as temperature versus composition. The observation of T_C yields the critical composition of the mixture.

Next, I will describe the solvent in more detail. The binary mixture was composed of water (dielectric constant $\epsilon \approx 80$) and 2,6-dimethylpyridine (IUPAC systematic name, C_7H_9N see Fig. 2.2, further denoted here as 2,6-DMP; $\epsilon \approx 7$), also known as 2,6-lutidine. The choice of the solvent is dictated by its well-studied physico-chemical properties [31–33] and T_C close to room temperature. The mixture's critical point is found at $T_C \approx 307$ K and 2,6-DMP volume fraction of $\phi \approx 0.302$. However, addition of ions is believed to modify hydrogen bonding and affect the bulk properties [34]. In order to gain a deeper understanding of the effects caused by different types of ions, I determined phase diagrams for the solvent with added either potassium chloride (KCl) or quaternary ammonium bromides ($[C_nH_{2n+1}]NBr$, $n = 2 \dots 7$).

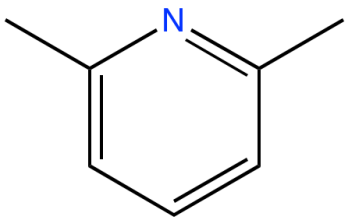

Figure 2.2: Molecular structure of 2,6-dimethylpyridine.

Criticality of the solvent

For critical solvents, i.e. solvents at the critical composition ϕ_C near T_C, approaching the critical temperature gives rise to the emergence of critical fluctuations. The closer to the

critical point, the larger those spatial fluctuations become [35]. The extent of the density fluctuations close to the critical point is described by the bulk correlation length ξ, which diverges at the critical point. Thus, ξ is strongly temperature dependent and close to the T_C follows the three-dimensional Ising universality class as $\xi = \xi_0(\Delta T/T_C)^{-\nu}$ [15, 36]. Here, $\nu \approx 0.63$ is the critical exponent and $\Delta T = T_C - T$. ξ_0 is a sample-dependent constant, which has been found to be $\xi_0 = 0.20 \pm 0.02$ nm for the water and 2,6-DMP mixture [6, 31].

2.2 Choice of salts

Potassium chloride

For experiments with hydrophilic salt, I chose potassium chloride (KCl) for two reasons. First, according to Ref. 23, chloride is strongly hydrophilic, whereas potassium has a weaker preference for water over the organic component (2,6-DMP). Second, from the technical point of view of the applied grazing-incidence x-ray fluorescence, it is crucial to be able to monitor both ions' signals simultaneously. Indeed, this is possible as characteristic fluorescence lines for both ions are relatively close spaced in energy. The experimental techniques will be introduced in Chapter 3.

Tetra-n-alkylammonium bromides

In the part of the investigation on mesoscale ordering, I used a salt series containing symmetrical quaternary ammonium bromides. The reason of choice is as follows. Since the first in the series, tetraethylammonium bromide consists of small cation and anion, the successive elongation of side-chains up to seven carbon atoms in tetraheptylammonium bromide will result in salt built of significantly larger cation than anion. Also, the short hydrocarbon-chained compound (Et_4NBr) is still hydrophilic, while the longer hydrocarbon-chained (Hep_4NBr) will exhibit increased cation's hydrophobicity [23]. I expect the quaternary ammonium cations' data to depend on the length of attached alkyls [37]. For simplicity, I further denote these sample sets as C2 ... C7, based of the number of carbon atoms in side-chains. Fig. 2.3 displays the schematic size difference between the Et_4N^+ and the Hep_4N^+ cations.

2.3 Phase behavior of the solvent

Let's now focus on the experimental procedure of determining the phase diagram for (i) the pure binary solvent, (ii) with the addition of inorganic simple salt, potassium chloride (papers **I, II**), and (iii) with addition of symmetrical quaternary ammonium bromides (paper **III**).

Phase diagram determination

First, I prepared the solvent containing water and 2,6-DMP at 2,6-DMP volume fractions to be within $\phi = 0.15 \ldots 0.60$. I chose to vary the 2,6-DMP volume fractions by $\Delta\phi = 0.05$ in order to capture the expected location of ϕ_C [31]. Furthermore, this span of volume fractions should capture the eventual deviation in the critical point upon the addition of salt. Next,

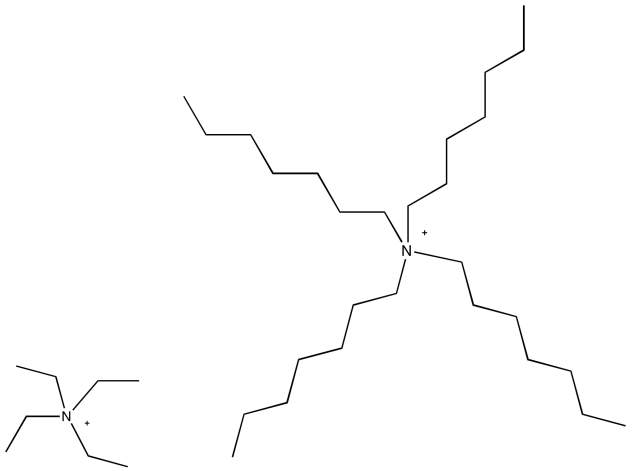

(a) Et_4N^+ (b) Hep_4N^+

Figure 2.3: Structure of cations: (a) tetraethylammonium and (b) tetraheptylammonium.

I transferred all samples into 75 × 10 mm glass test tubes, which were sealed (see Fig. 2.4) and placed in a temperature-controlled water bath (Grant Instruments). I increased the temperature from 293 to about 317 K in steps of 0.1 K (the temperature stability was ≈ 0.1 K). I allowed the samples to equilibrate for ≈ 15 minutes. Finally, I determined the coexistence points shown in Fig. 2.5 visually, based on the onset of critical opalescence.

Determining the phase diagram of the neat binary mixture was a first crucial step as a reference for those samples containing salt. After ensured reproducibility of the data for the neat mixture, I turned to verify the cases with different salts. For potassium chloride (KCl), I followed the same experimental procedure as described above. The studied samples contained different concentrations of added salt: 10, 20, 50 and 100 mM. The phase diagram of the water and 2,6-DMP mixture containing quaternary ammonium compound was yet to be determined experimentally. Thus, I determined the coexistence points in this system, in order to obtain deeper insight of eventual effects of those ions. For this experimental set, I followed the described method for the pure solvent. I began with mixing water and 2,6-DMP at a few of the 2,6-DMP volume fractions $\phi = 0.10 \ldots 0.60$, varied by $\Delta\phi = 0.10$. I prepared six sample sets, one for each of the quaternary ammonium bromide C2 ... C7. I increased the temperature by 0.5 K (giving the experimental error of 0.5 K) and allowed ≈ 20 minutes for equilibration.

I will now discuss shortly the effects of salts on the phase diagram of my experimental system.

2.4 Salt effect on the phase behavior

The phase diagram for the solvent containing inorganic simple salt, potassium chloride, is shown in Fig. 2.5. I found it to be in line with previous studies [31, 33]. The addition of hydrophilic potassium chloride has two effects on the coexistence line. First, I observe a decreasing of the critical temperature, for example 10 mM KCl lowers T_C by about 2 K [38].

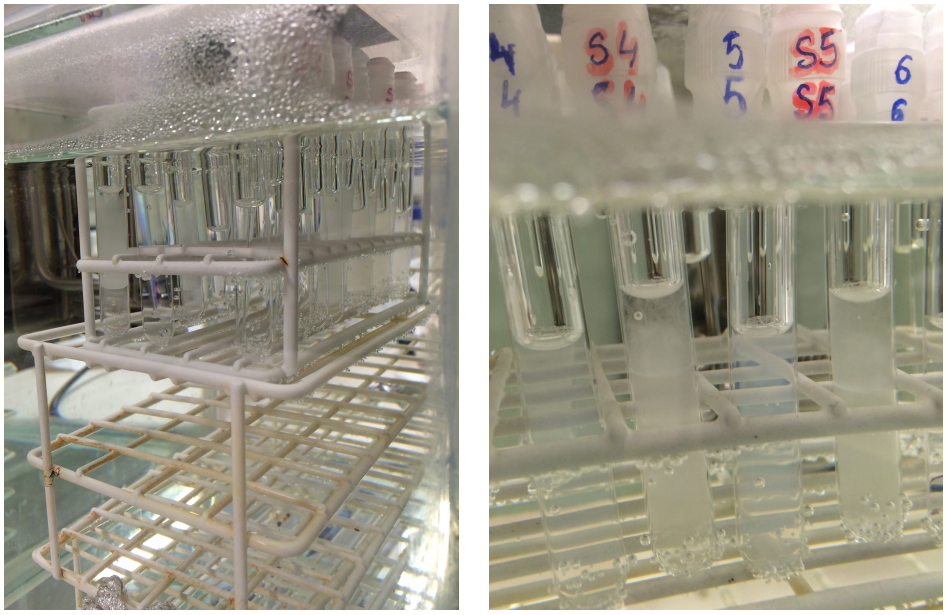

(a) Experimental set-up. (b) Samples in the water bath.

Figure 2.4: Phase diagram determination. (a) View of sample sets in water bath; (b) enlarged view over few samples reaching phase separation.

Second, I observed a shift in the critical composition towards larger ϕ values. All these changes are salt-concentration dependent causing enlargement of the two-phase region [34].

In papers **I** − **II** I focused on the solvent with $\phi = 0.3$ of 2,6-DMP and 10 mM KCl, as the bulk correlation length ξ is known to not be affected by this salt concentration [6].

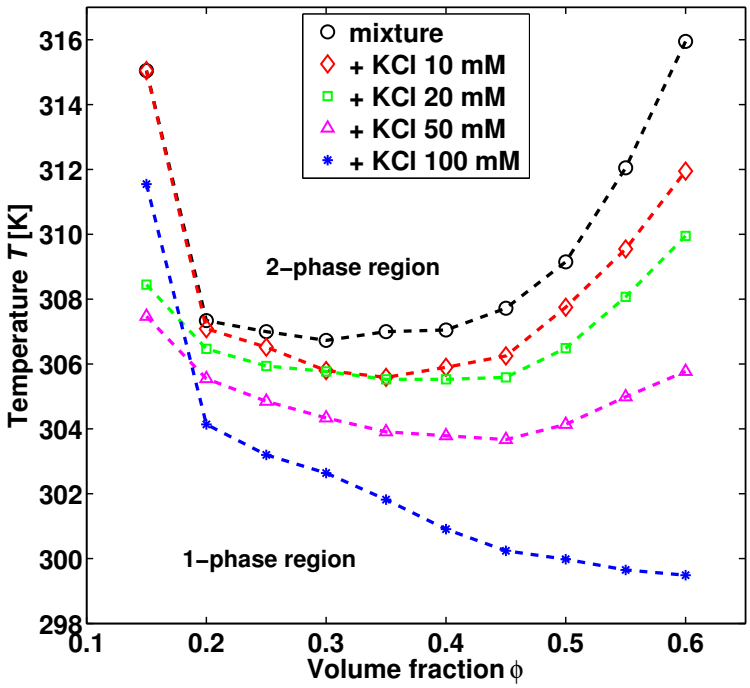

Figure 2.5: Determined coexistence points as a function of 2,6-DMP volume fraction ϕ. Experimental data for the neat mixture of water and 2,6-DMP (black circles) and containing potassium chloride (color symbols) with different concentrations.

In Fig. 2.6 the coexistence points for the mixture with added 10 mM of the symmetrical quaternary ammonium salts is presented. This bromide salt series is built of tetraalkyl homologues compounds differing by having one more -CH_2 group, i.e. from C2 up to C7. Interestingly, I do not observe any significant changes in the phase behavior of the system. This is opposite to the simple hydrophilic salts and to previously investigated compounds containing hydrophilic and hydrophobic ions. The binary mixtures with surfactants and antagonistic salts have already been known [8, 39] to exhibit concentration-dependent diminishing of the two-phase region. Additionally, the shift of critical composition and increase of T_C has been found. None of these is observed in my experimental data for C2...C7 salts.

In fact, this finding facilitated further experimental studies that I conducted at a SAXS beamline (paper **III**). In this research project, the binary solvent at unchanged ϕ_C was prepared with added C2...C7 in a concentration of 10 mM.

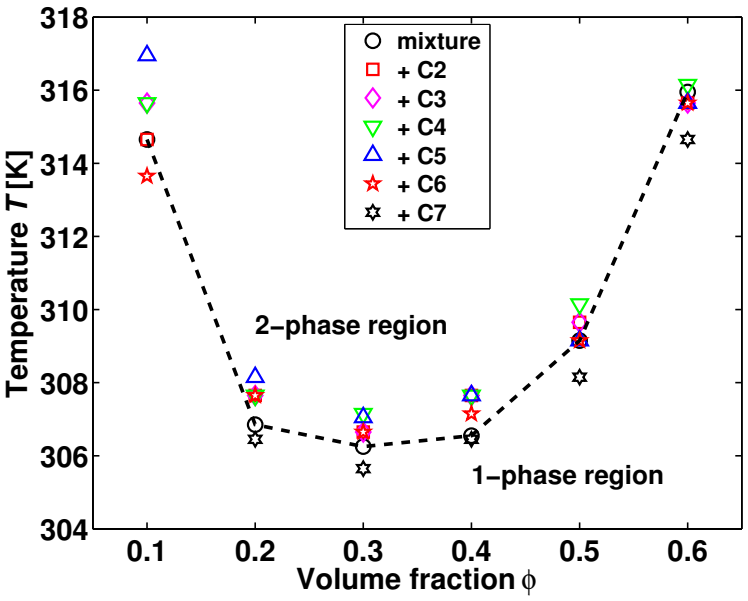

Figure 2.6: Phase diagram for the system of water and 2,6-DMP with added quaternary ammonium salt. The measured phase separation temperature vs. varied volume fraction of 2,6-DMP. Black circles show the data for the pure solvent, while other-shaped symbols depict samples with 10 mM salt. Figure taken from paper **III**.

It is worth to mention that one of the samples, C7 at low 2,6-DMP fraction of $\phi = 0.1$, became turbid directly after mixing all chemicals at room temperature. Thus, it was impossible to determine the phase separation point. C7 is the only compound of all series which does not dissolve in water. At the same time, it is soluble in all water-2,6-DMP mixtures with $\phi \geq 0.2$ and $\phi \leq 0.6$. The reason of such turbid appearance might origin from a spontaneous formation of the 2,6-DMP in water emulsions [40].

2.5 Surface activity of tetra-n-alkylammonium bromides

It is clear that in the case of tetra-n-alkylammonium bromides, elongation of the hydrocarbon side chains gives rise to hydrophobicity of $(C_nH_{2n+1})N^+$ ions. The tetraethylammonium ion is still hydrophilic [23] while the long homologues acquire a preference to organic phases. This feature can be identified with the surface activity of the studied salt series. Surface tension (γ) data have been reported previously for only the first four homologues of the compounds in focus here [41, 42]. Therefore, I conducted verification surface tension measurements on aqueous solutions of 10 mM ammonium salts using the ring method (Sigma 70 Tensiometer, Crelab Instruments).

In table 2.1, I show the surface tension data for the C2...C7 series. The first three homologues have a negligible effect on changing the surface tension of water ($\approx$ 70 mN/m). The compounds with further elongated side hydrocarbon chains, show gradual decreasing of γ.

More specifically, 10 mM of C5 and C6 decreases the surface tension of water by ≈ 10 and ≈ 25 mN/m, respectively.

Also, these types of compounds manifest their effecting surfactant-like behavior by assembling into micelles. Even for short-chained ammonium cations, critical micelle concentration has been detected previously in concentrated solutions [42, 43].

Compound	C2	C3	C4	C5	C6
γ [mN/m]	≈ 70	≈ 70	≈ 70	≈ 60	≈ 45

Table 2.1: The determined surface tension for the series of the 10 mM symmetrical quaternary ammonium bromides (C2 - C6) aqueous solutions. C7, the last one in the series, does not dissolve in water.

3 Synchrotron-based experimental techniques

In the experimental work, I utilized two synchrotron-based techniques: grazing-incidence x-ray fluorescence (GIXF) and small-angle x-ray scattering (SAXS). Next, I will briefly introduce synchrotron radiation, GIXF, SAXS, and the instruments used.

3.1 X-rays and synchrotron radiation

X-rays are part of electromagnetic radiation [44, 45], with wavelengths comparable to the atomic scale.

Interaction of the x-ray radiation with matter underlay the many available synchrotron-based techniques. To this interaction, the following processes are included: photoelectric absorption, elastic and inelastic scattering. If the sample is irradiated with x-rays, part of the radiation will pass through unchanged. However, the other part will be absorbed and this process obeys the Lambert-Beer law for linear absorption, $I = I_0 \exp(-\mu z)$. Here I_0 is the intensity of the incoming beam, I is the transmitted one and μ is the linear absorption coefficient. The length over which the radiation passes is given by z and can be understood as the sample thickness. Thus, the transmitted radiation decays exponentially with the travelled length z. What happens if an atom in the sample absorbs x-ray radiation? First, high energy x-rays may cause expelling of a core electron after which two paths are possible: fluorescence or Auger electron emission. Fluorescence occurs when the core vacancy is filled with an outer-shell electron via a relaxation process leading to the emission of fluorescent radiation. The resulting characteristic x-ray emission lines are specific for each element. In contrast, Auger emission is a non-radiative process. The vacant hole is filled by an outer electron and additionally a second (Auger) electron is emitted. Second, besides the photoabsorption processes, some of the x-rays will be scattered by the sample. The scattering is elastic, if the scattered wave has the same energy as the incident one. This is opposite to inelastic scattering with the scattered photon having changed energy. The small-angle x-ray scattering technique rely on the elastic scattering of x-rays by the sample.

The refractive index of a material can be written $n = 1 - \delta + i\beta$ for x-rays. δ describes refraction being usually in order of $\approx 10^{-6}$ and β is the absorption index being the imaginary part of the total index of refraction (β is much smaller than δ). Because of n in materials is less than unity, the x-ray radiation passing an air-material interface is refracted to small angles. For incidence angles $\theta < \theta_C$ the total external reflection occurs [44–46] and an evanescent standing wave penetrates the material's surface in a few nm depth. This is exactly what happens in

a grazing-incidence experiment when x-rays travel from less dense medium (vacuum) to more dense medium (e.g. liquid sample). Numerical value of the critical angle for the total external reflection can be obtained from $\theta_C \approx \sqrt{2\delta}$.

Due to the need of using beams with high intensity, all experiments were carried out at synchrotron facilities. A synchrotron is an electron accelerator with a circular storage ring, which delivers x-ray beam to end stations designed for a variety of experiments. I now turn to describing the experiments: principles and beamlines.

3.2 Grazing-incidence x-ray fluorescence

GIXF is an element specific and surface-sensitive spectroscopic technique. The incident x-rays hit the liquid-vapor interface of the sample at very shallow angles, leading to an evanescent wave propagation (at $\theta < \theta_C$). This evanescent wave penetrates the surface and excites the chemical species present in the sample. Consequently, the excited elements emit fluorescence according to their characteristic fluorescence lines. This is shown in Fig. 3.1a as a simplified schematic picture explaining the idea behind the GIXF experiment. The emitted fluorescence is recorded by an energy-dispersive detector. By changing the incidence angle the depth sensitivity is tuned. For angles below θ_C the sample is probed up to a depth of about five nm, thus providing access to interfacial ion distributions, whereas above θ_C the bulk sample is probed. In Fig. 3.1b the x-ray penetration depth (Λ) is plotted versus the incidence angle, visualizing the probing depth.

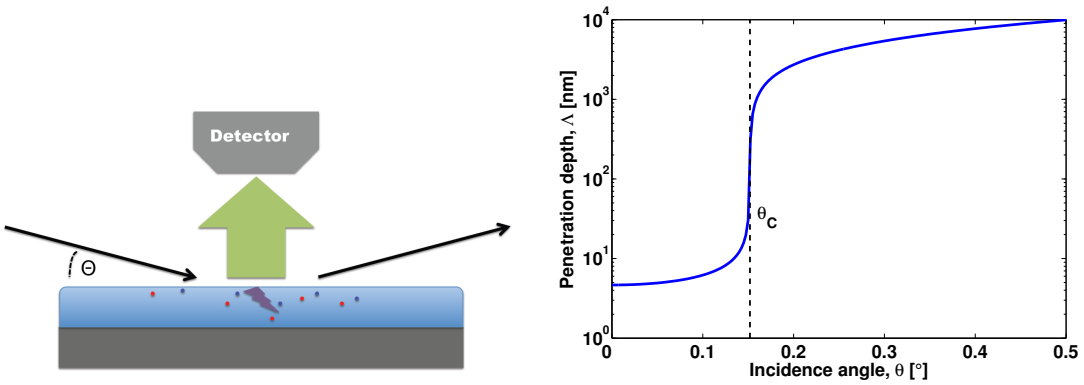

(a) GIXF experiment idea: schematic layout.

(b) Penetration depth into sample.

Figure 3.1: (a) The schematic layout of the sample. The black arrows represent the x-rays hitting the vapor-liquid interface under grazing angle θ (left arrow) and the reflected x-rays (right arrow). An evanescent wave propagates under the sample's surface and excites chemical species. Next, these species emit fluorescent radiation (green arrow), which is measured by the detector placed above the surface. (b) Penetration depth Λ plotted vs. incidence angle θ. By varying θ, the probing depth into the liquid sample is tuned: for $\theta < \theta_C$ sensitivity to few nm is obtained, whereas for $\theta > \theta_C$ the bulk is probed. Figure (a) is taken from paper **II**.

The GIXF technique has been described elsewhere [47–49] and recently reviewed [50]. GIXF has been applied to studies of oxidation in phospholipid monolayers with presence of

ionic buffer [51] or to determination of ion profiles in bacterial lipid surfaces [52]. Moreover, this experimental method has provided resolved surface excesses of ions in simple aqueous electrolytes [4]. I further develop the later approach for application to binary mixtures in paper **II**.

GIXF data analysis and calculation of the fluorescence intensities

The collected GIXF data are exemplified in Fig. 3.2a. Clearly, the characteristic K^+ and Cl^- Kα, Kβ lines are identified, based on tabulated energy values [53]. I will now briefly describe the raw data processing. First, a linear background was subtracted followed by fitting of Gaussians to the fluorescence peaks. This can be understood from Fig. 3.2a demonstrating the fitting routine. At the last step the data are corrected by the monitor and filters foil values, leading to GIXF curves as shown in Fig. 3.2b.

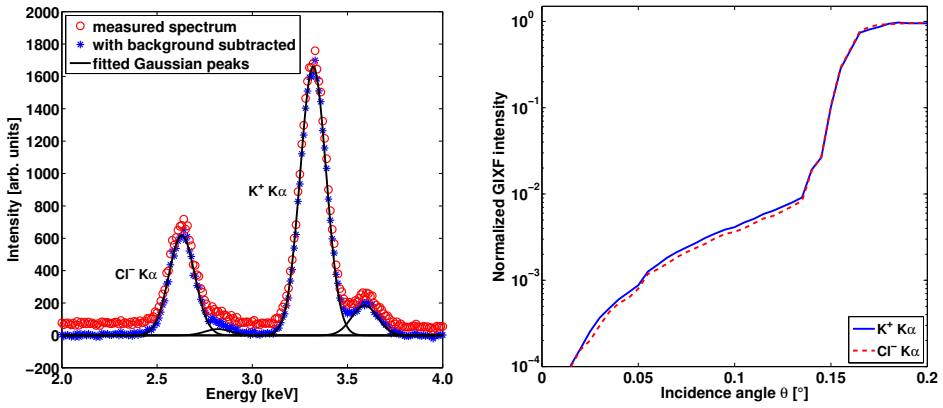

(a) Fluorescence KCl spectrum. (b) GIXF intensity.

Figure 3.2: (a) A measured fluorescence spectrum (red circles) including potassium and chloride characteristic Kα (respective 3.3 keV and 2.6 keV) and Kβ (respective 3.6 keV and 2.8 keV) lines, measured at $\theta = 0.17°$. After background subtraction (blue stars), Gaussians are fitted (black lines). (b) Normalized GIXF K^+ (blue) and Cl^- (red dashed) curves after data processing. This figure is taken from paper **II**.

After the data processing procedure, the fluorescence collected as a function of incidence angle for each ionic specie, $I_\pm(\theta)$, is described by the integral

$$I_\pm(\theta) = C_\pm(\theta) \int_0^\infty I_0(z,\theta) n_\pm(z) \exp(-\mu_\pm z) dz. \tag{3.1}$$

In order to obtain $I_\pm(\theta)$, I defined the depth-dependence via the $z-$axis and set the liquid-vapor interface of the sample to be at $z = 0$ with the liquid phase found at $z \geq 0$. I determined the illumination profile $I_0(z,\theta)$, by making use of the so-called matrix method [54]. After obtaining the $I_0(z,\theta)$ together with the ion number density $n_\pm(z)$ [20], I was able to determine the $I_\pm(\theta)$ using $\mu_\pm$, the tabulated linear absorption coefficient [55] for respective ion fluorescence line. The prefactor $C_\pm$ includes other terms such as quantum efficiency and acceptance angle of the detector, which do not depend on ion concentrations.

Matrix method

In order to model GIXF curves based on theoretically calculated ion profiles (paper **I**), I determined in the first place the illumination profile $I_0(z, \theta)$. For this purpose, I solved Maxwell's equations for a stratified medium using the matrix formalism [54] with tabulated optical constants [56] as input. In this approach, I imagine the sample to be built as layered medium in a following manner. The vapor phase is the upper phase $j = 0$, next the liquid medium is sliced into thin layers starting from j and followed by $(j + 1) \dots$ up to the total $N + 1$ layers. The last one is simply the bulk liquid. Additionally, the coordination system is set such that the $x-$axis is parallel to the sample's surface, with the $z-$axis being perpendicular and taking positive values into the depth of the sample. Therefore, at z_j I find the interface between layers j and $j + 1$.

Now, the Maxwell's equations for the layered medium can be written in terms of forward and backward propagating waves,

$$E^+(z) = E_j^+(z) \exp(ik_{zj}(z - \sum_{i=1}^{j-1} d_i)) \tag{3.2}$$

and

$$E^-(z) = E_j^-(z) \exp(-ik_{zj}(z - \sum_{i=1}^{j-1} d_i)). \tag{3.3}$$

Here E_j^+ and E_j^- denote the amplitudes at the jth layer's interface and k_{zj} the z-component of the wave vector at that interface. The electric field intensity in the sample at depth z is then

$$|E^+(z) + E^-(z)|^2. \tag{3.4}$$

The electric field is determined by successive multiplication of the so-called propagation matrices C_j, which describe the field propagation through the layer j, while ensuring continuity of the electric and magnetic fields. The propagation matrix, when the electromagnetic wave travels from layer j to $j + 1$ is given by

$$C_j = \begin{pmatrix} \exp(-ik_{z,j}d_j) & r_j \exp(-ik_{z,j}d_j) \\ r_j \exp(ik_{z,j}d_j) & \exp(-ik_{z,j}d_j) \end{pmatrix} \frac{1}{t_j}, \tag{3.5}$$

with r_j and t_j being the Fresnel coefficients defined as

$$r_j = \frac{k_{z,j} - k_{z,j+1}}{k_{z,j} + k_{z,j+1}} \tag{3.6}$$

and

$$t_j = \frac{2k_{z,j}}{k_{z,j} + k_{z,j+1}}. \tag{3.7}$$

The incident and reflected waves are E_0^+ and E_0^- (vapor) respectively, which after N layers can be described as E_N^+ and E_N^-. This can be given in a form of matrix equation

$$\begin{pmatrix} E_0^+ \\ E_0^- \end{pmatrix} = \frac{C_1 C_2 \cdots C_{N+1}}{t_1 t_2 \cdots t_{N+1}} \begin{pmatrix} E_{N+1}^+ \\ E_{N+1}^- \end{pmatrix}. \tag{3.8}$$

Now, we denote D_0 as the product of all propagation matrices

$$D_0 = C_1 C_2 \cdots C_{N+1} = \begin{pmatrix} a & b \\ c & d \end{pmatrix}. \tag{3.9}$$

Note that due to lack of reflections from the bulk phase, we get $E^-_{N+1} = 0$ and C_{N+1}, will be a unit matrix. The total reflection and transmission coefficients are related to E^+_0 and E^-_0, and can be expressed with the help of the D_0 matrix elements as

$$r = \frac{E^-_0}{E^+_0} = \frac{c}{a} \tag{3.10}$$

and

$$t = \frac{E^+_{N+1}}{E^+_0} = \frac{t_1 t_2 \cdots t_{N+1}}{a}. \tag{3.11}$$

For finding the $E^\pm_j$, we can split Eq. (3.8) into two,

$$\begin{pmatrix} E^+_0 \\ E^-_0 \end{pmatrix} = \frac{C_1 C_2 \cdots C_{j-1}}{t_1 t_2 \cdots t_{j-1}} \begin{pmatrix} E^+_j \\ E^-_j \end{pmatrix} \tag{3.12}$$

and

$$\begin{pmatrix} E^+_j \\ E^-_j \end{pmatrix} = \frac{C_j C_{j+1} \cdots C_{N+1}}{t_j t_{j+1} \cdots t_{N+1}} \begin{pmatrix} E^+_{N+1} \\ E^-_{N+1} \end{pmatrix}. \tag{3.13}$$

Next, using the definition of D_j matrix, similar to previous D_0,

$$D_j = C_j C_{j+1} \cdots C_{N+1} = \begin{pmatrix} a_j & b_j \\ c_j & d_j \end{pmatrix}, \tag{3.14}$$

we get the following expressions

$$E^+_j = \frac{a_j}{t_j t_{j+1} \cdots t_{N+1}} E^+_{N+1} \tag{3.15}$$

$$E^-_j = \frac{c_j}{t_j t_{j+1} \cdots t_{N+1}} E^+_{N+1}. \tag{3.16}$$

By substituting Eq. (3.11) in Eqs. (3.15) and (3.16), we obtain expressions binding E^+_j and E^-_j with E^+_0

$$E^+_j = t_1 t_2 \cdots t_{j-1} \frac{a_j}{a} E^+_0 \tag{3.17}$$

$$E^-_j = t_1 t_2 \cdots t_{j-1} \frac{c_j}{a} E^+_0. \tag{3.18}$$

Finally, the electric field intensities at position z_j are obtained by making use of Eq. (3.2), (3.3) and Eq. (3.4) together with Eqs. (3.17) and (3.18). The calculated illumination profile $I_0(z, \theta)$ is presented for a few chosen angles in Fig. 3.3.

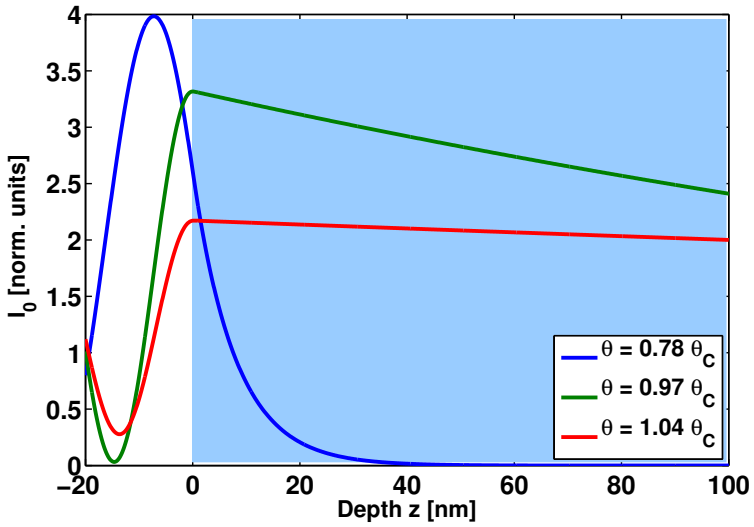

Figure 3.3: The illumination profile plotted as a function of the sample's depth z (in nm), calculated utilizing the matrix approach. Three different angles are chosen: smaller than θ_C (blue line), close to θ_C (green line) and larger than θ_C (red line). At $z = 0$ we placed the vapor-liquid interface, vapor is found at $z < 0$ (white area) whereas liquid is found at $z > 0$ (light blue-colored area). This plot further visualizes the fact that angle variation during the experiment provides the depth sensitivity.

The same results can be obtained with Parratt's recursive method [44,46,57]. This fact was helpful during the script writing work, where I could check the calculation result by plotting the angle-dependent reflectivity curve. I show in Fig. 3.4 the reflectivity calculated by these two approaches.

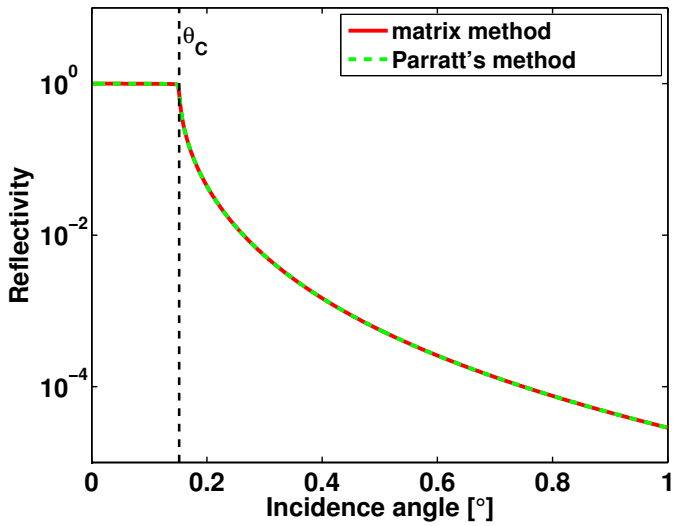

Figure 3.4: Calculated reflectivity curve vs. incidence angle using Parratt's recursive method (green dashed line) and the matrix method (red line). It is easily seen that both approaches provide the same result.

Beamline ID10: GIXF at ESRF

The GIXF experiments (papers **I, II**) were carried out at the beamline ID10 of the European Synchrotron Radiation Facility (ESRF, France) [58]. This particular beamline offers a wide range of techniques that can be applied for interface studies [59]. A schematic layout of the beamline is shown in Fig. 3.5, where I focused on the experimental hutch 1 (EH1). In fact, the GIXF experiments are performed with EH1 being in operation only, as only one experimental hutch is designed to be in operations mode at time [59].

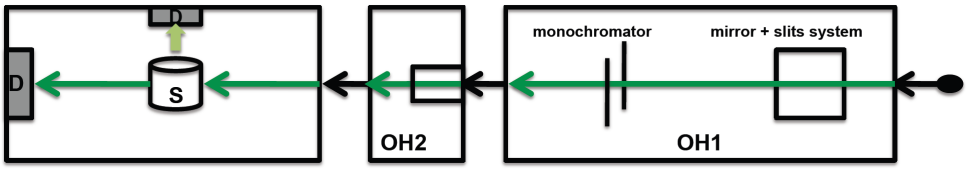

Figure 3.5: A very simplified scheme of the ID10 beamline layout including two optic hutches and the experimental hutch. Starting from the right, x-ray radiation passing the shutter enters first optic hutch (OH1), which contains a system of slits, mirrors and monochromator. Next, the radiation passes through the second optic hutch (OH2) and is directed by mirrors and slits to the experimental hutch (last box on the left). Here, a schematic position of sample (S) and detectors (D) available at the beamline are shown. For creating this schematic picture, I used the ID10's layout [59].

I used an incident energy of 8 keV, which allowed for simultaneous recording of potassium and chloride characteristic Kα lines ($\sim$ 3.3 keV and respectively $\sim$ 2.6 keV). The fluorescence spectra were recorded using the energy-dispersive detector Vortex (SII NanoTechnology) [60]. The liquid sample was kept in a custom-made steel sample cell (with a diameter of 97.5 mm and depth of 2 mm) with Kapton foil windows (0.0127 mm thick). During measurements, a helium atmosphere was kept inside the cell in order to minimize a potential parasitic argon fluorescence. In Fig. 3.6a I present a photograph of the experimental set-up including sample container and Fig. 3.6b displays enlargement of the same set-up.

I collected the data at several temperatures ($T \approx 295 \ldots 301$ K with a temperature stability about ≈ 0.1 K).

3.3 Small-angle x-ray scattering

SAXS experiments were conducted in transmission geometry. In practice the sample was irradiated with x-ray beam and the scattered radiation was recorded at the detector as 2D pattern. Here, the scattered angles are very small (about $0.1^\circ \ldots 10^\circ$), providing information about nanoscale structures in the sample. The inhomogenous features in the mesoscale fluid sample can be probed based on electron density contrast [44, 61, 62].

The scattered intensity is detected as a function of scattering vector q, which can be understood as a propagation difference between incident and scattered waves [61,62]. The scattering vector is related to the scattering angle (2θ) and to the wavelength (λ) as $q = (4\pi/\lambda)\sin\theta$. Importantly, the small-angle scattering intensity can be written $I(q) = \left|\int_V \rho_{sc} e^{i\mathbf{q}\cdot\mathbf{r}} dV\right|^2$. Here,

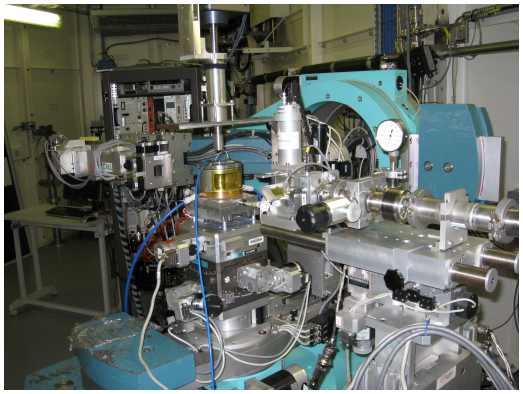

(a) GIXF: view on sample table.

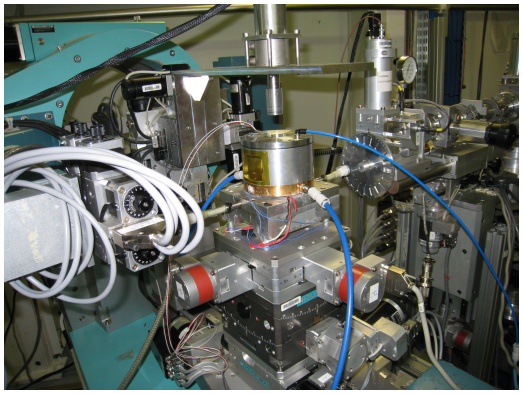

(b) GIXF experimental set-up at ID10.

Figure 3.6: (a) Photograph of the GIXF set-up, taken inside the experimental hutch. (b) Enlargement showing the sample container. The fluorescence detector can be seen above the sample container.

ρ_{sc} is the scattering length containing the information about the deviation in the average electron density in a volume element V and $\mathbf{q} \cdot \mathbf{r}$ is a phase difference [44].

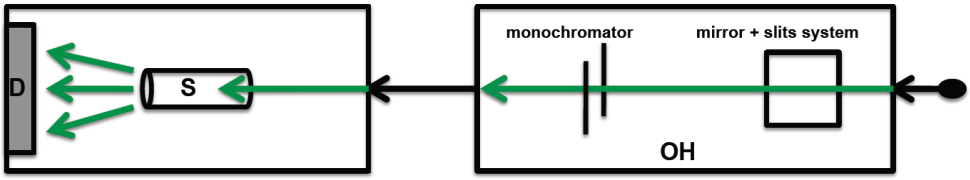

Figure 3.7: A similar beamline layout as in Fig. 3.5, except for the SAXS experiment based on MAX-Lab's I911-4. Starting from the right, x-ray radiation passes the optic hutch, then the monochromatic beam is lead to the small experimental hutch. Finally, the liquid sample (S) is irradiated, and the scattering pattern can be recorded on the detector (D).

SAXS data analysis

Initial data reduction took place on-site at each SAXS beamline, by radial integration of the 2D patterns using the available software. For further data analysis, I subtracted the background taking into account the volume fractions of water and 2,6-DMP with respective electron densities. The last stage in data treatment included fitting to the Ornstein-Zernicke (OZ) model and the generalized OZ model in order to obtain parameters such as the bulk correlation length ξ or interaction contrast g (paper **III**). The latter will be discussed briefly in Chapter 4.

The scattered intensity $I(q)$ (decreasing function of q) is related to the correlation length, according to the OZ model $I(q) \propto 1/(1 + q^2\xi^2)$ [36] and gives good results when applied to the neat solvent or solvent with simple inorganic salt.

Beamline X12SA: cSAXS at SLS

In this thesis work, the SAXS experiments were carried out at two different facilities. The study published in paper **IV** was conducted at the cSAXS beamline (X12SA) of the Swiss Light Source. This beamline is dedicated to SAXS of liquid and solid samples [63]. I used the incident x-ray energy of 12.4 keV, corresponding to a wavelength of $\lambda = 1.00$ Å. The x-rays impinged normal to the symmetry axis of the cylindrical sample container with the scattered x-rays being detected 7 m behind the sample stage using PILATUS 2M (Dectris) [64]. Also, the set-up included an evacuated flight tube in order to reduce the parasitic scattering. The samples prepared for measurements can be seen in Fig. 3.8.

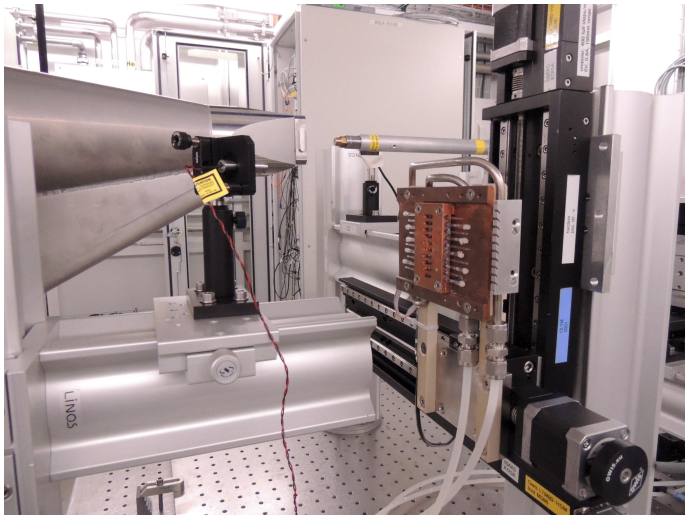

Figure 3.8: Photograph taken at the SLS. The set-up inside the experimental hutch of X12SA. The filled capillaries inserted in a coper holder can be seen in the center.

I kept the liquid sample in a thin-walled (10 μm-thick) 1.5 mm-diameter borosilicate glass capillary mounted on a copper-made sample holder. In paper **IV**, I focused on the measurements at eight different temperatures approaching the T_C of the water-2,6-DMP system. The sample holder provided the temperature stability of ± 0.05 K.

Beamline I911-4: SAXS at MAX-Lab

Another SAXS experiment (paper **III**) was carried out at the MAX-Lab facility's (Sweden) beamline I911-4 [65]. Here, I used an x-ray wavelength of $\lambda = 0.91$ Å (13.6 keV) and the scattered x-rays were recorded 1.9 m behind the sample using the PILATUS 1M detector (Dectris) [66] available at the beamline. Fig. 3.9 displays the view inside the experimental mini-hutch, especially (Fig. 3.9b) the placement of the capillaries.

During this experiment, I used a quartz glass capillary as the sample container. All measurements were conducted in the same capillary, where the process of sample replacement included cleaning and drying. Data for each sample were recorded for three different temperatures below T_C of the system containing quaternary ammonium bromide.

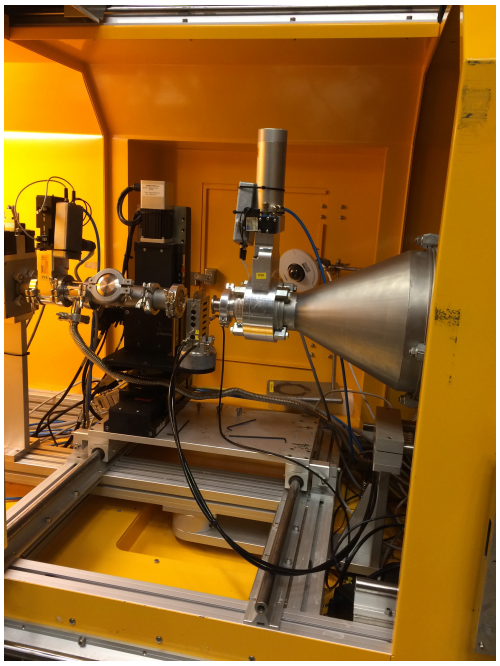

(a) Experimental mini-hutch at I911-4.

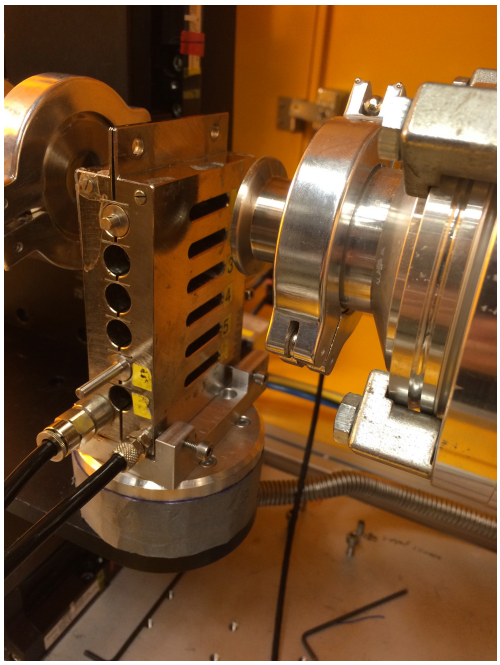

(b) Enlarged view of (a).

Figure 3.9: (a) View inside the I911-4 yellow mini-hutch with the set-up used during SAXS measurements. (b) Enlargement showing the capillaries holder.

4 Summary of the research

In the following chapter, I will summarize the four papers being part of this thesis work.

4.1 Paper I

Microscopic segregation of hydrophilic ions in critical binary aqueous solvents

In paper **I** [67] I address experimentally the asymmetric solvation of hydrophilic ions in the critical binary aqueous mixtures. For this purpose, I probed ion distributions at the liquid-vapor interface of the critical solvent composed of water and 2,6-DMP using grazing-incidence x-ray fluorescence (GIXF). I collected data for 10 mM of added hydrophilic potassium chloride (KCl) [23].

The obtained results can be outlined as follows. First, the data provide clear experimental evidence for microscopic segregation of hydrophilic ions in the aqueous binary solvent. In order to support this finding, I show in Fig. 4.1 the relative GIXF intensity I_+/I_- as a function of incidence angle θ. The relative intensity is simply the potassium cation intensity I_+ divided by the chloride anion intensity I_-. It is apparent that for small incidence angles, i.e. $\theta < \theta_C$, this relative intensity is larger than unity. Therefore, the I_+/I_- shows that I observed a relative excess of K^+ ions comparing to Cl^- at the interface.

Second, the GIXF data indirectly yield interfacial adsorption of one of the two liquid components. In the binary system, the liquid component with significantly lower surface tension is expected to adsorb at the mixture's surface [68, 69]. This is exactly the case of my binary mixture, where the difference between water and 2,6-DMP surface tensions is $\Delta\gamma \approx 40$ mN/m. The preferentially adsorbed 2,6-DMP causes the K^+ excess based on it's weak preference for water, comparing to the Cl^- strong preference for water [23].

Additionally, Fig. 4.1 displays modeled GIXF data using solvation contrasts $f_\pm$, for each ion, which is the ion's free energy of transfer from water to non-aqueous liquid, in this study 2,6-DMP. The applied model calculations, show only qualitative agreement with the cations excess. There are several possible reasons for this. The cation's solvation contrast f_+ affects the difference between ion interfacial distribution. In particular, literature data lack information about good estimation of $f_\pm$ for the 2,6-DMP, and could be different than adopted in the theoretical model [20]. For the modeling, I used the mean-filed values for 2,6-DMP composition, which might affect the calculated profiles. Also, adding ions could influence the liquid components' adsorption preferences, although this is indicated as a minor effect [6, 20].

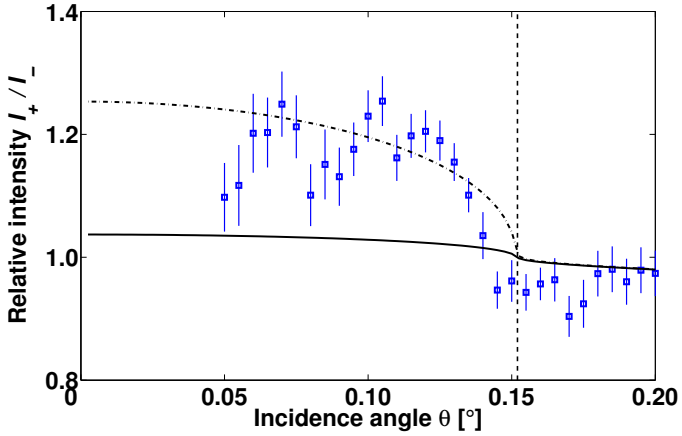

Figure 4.1: Relative GIXF intensity I_+/I_- plotted as a function of incidence angle θ. Experimental data (blue symbols) for the water-2,6-DMP system, measured 8 K below the T_C. The theoretical modeling has been done based on Ref. 20 using two approaches for cation solvation contrast: $f_+ = 2.5$ (black solid line) or $f_+ = 0$ (dashed-dotted line). The critical angle, θ_C is indicated by the vertical dashed line. Figure taken from paper **I** [67].

This study indicates the importance of asymmetric ion solvation when describing the colloidal interactions in salt-containing critical solvents [6, 20, 22, 70].

4.2 Paper II

Relative adsorption excess of ions in binary solvents determined by grazing-incidence x-ray fluorescence

Paper **II** [71] is a continuation of the research project in paper **I**. I focus on presenting an experimental method for direct determination of the relative surface excess of solute species in binary solvents. I demonstrate this approach by probing the interfacial ion distributions using the GIXF technique. As in paper **I** [67], I obtained the enhancement of positive ions (K^+) at the interface of the binary solvent, with the further intention to quantify this effect.

I follow the previous application of GIXF for determining the ion surface excess $\Gamma_\pm$ in electrolyte solutions [4], where authors expanded GIXF intensity as a function of $\Gamma_\pm$. In paper **II**, I extend this idea for the use to my previously obtained relative intensity I_+/I_- and relate it to $\Gamma_\pm$ for both ions

$$\frac{I_+}{I_-} \approx \frac{1 + \alpha\Gamma_+/n_0}{1 + \alpha\Gamma_-/n_0}. \tag{4.1}$$

Here, $\Gamma_\pm$ is the excess adsorption of respective ion, n_0 denotes the bulk number density and α is a function of the normal component of the incident wave vector ($\alpha = 2Im(k_z)$). Next, I defined the relative surface excess $\Delta\Gamma \equiv \Gamma_+ - \Gamma_-$, which is simply the difference between the adsorbed cations and anions at the interface. Such defined $\Delta\Gamma$ is then approximated as

$$\Delta\Gamma \approx \frac{n_0}{\alpha}\left(\frac{I_+}{I_-} - 1\right). \tag{4.2}$$

I demonstrate that the $\Delta\Gamma$ gives value of $\Delta\Gamma \approx 5 \cdot 10^{15}$ ions/m^2, corresponding to one cation excess per ≈ 200 nm^2. The potassium cation excess has been confirmed for several temperatures, 295 . . . 301 K as shown in Fig. 4.2.

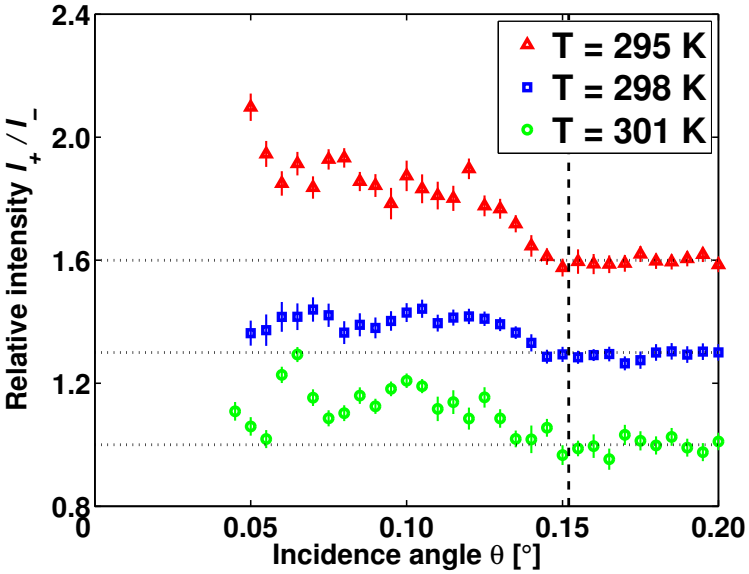

Figure 4.2: Relative GIXF intensity I_+/I_- vs. incidence angle θ recorded at several temperatures, $T = 295, 298$ and 301 K (symbols with different colors). The two upper curves are shifted vertically by a constant (blue squares by 0.3 and red triangles by 0.6). The critical angle θ_C is represented by vertical dashed line. Figure taken from paper **II** [71]

4.3 Paper III

Mesoscale ordering in binary aqueous solvents induced by ion size asymmetry

In this study (paper **III**) [72], I carried out a small-angle x-ray scattering (SAXS) in order to investigate the effect of ion size asymmetry on mesoscale ordering of a binary solvent. I focused on a series of sample sets with water-2,6-DMP mixture containing 10 mM of tetra-n-alkylammonium bromides, where the cations are ranging from short-chained tetraethylammonium to longer-chained tetraheptylammonium. The choice of these salts gave the possibility of obtaining results as a function of cation size. Essentially, by adding tetra-n-alkylammonium cations I obtained similar mesoscale structuring of my binary solvent as observed for the antagonistic salts [26]. I show the first experimental system demonstrating gradual build-up of mesoscale order with increasing ion size asymmetry in binary aqueous solvent.

This solvent's structuring behavior upon addition of salt, can be identified via fitting the data to the generalized OZ model [27–29]

$$I(q) \propto \frac{1}{1 + [1 - g^2/(1 + \kappa^{-2}q^2)]q^2\xi^2}, \tag{4.3}$$

with g being the interaction contrast and $\kappa^{-1} \approx 2.59$ nm (for the used concentration and solvent composition) the Debye screening length. Here, the g represents the contrast be-

tween cation-solvent and anion-solvent interactions. The $I(q)$, q and ξ denote as usual the experimental SAXS intensity, scattering vector and bulk correlation length.

Importantly, g is related to the salt-induced mesoscale ordering of the solvent [20, 27, 28]. For increasing g values, the solvent's ordering evolves and is related to the mesoscale ordering. Modulus of $|g|$ increases together with ordering of the solvent, when $|g| > 1$ a shoulder (peak) occurs [24, 39] in structure factor. In Fig. 4.3 I plotted the modulus of interaction contrast $|g|$ versus the cation size in my salt series C2 ... C7. I observe the increase of $|g|$ as the cations become larger. This indicates the systematically evolving order of my solvent. Notably, the cation-to-anion size difference in antagonistic sodium tetraphenylborate is in similar order to that in C7, $|g| > 1$. $NaBPh_4$ is known to induce mesoscale structuring [8,24,26]. Concurrently, I am not able to exclude the effect of preferential solubilization of large hydrophobic ions in non-aqueous solvent, which could contribute to $|g|$.

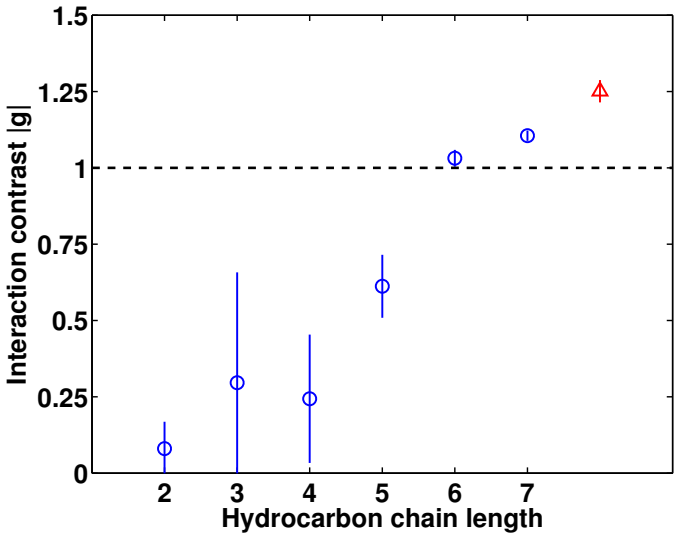

Figure 4.3: Interaction contrast $|g|$ vs. the length of side hydrocarbon chains. Obtained by the fitting procedure of SAXS data to generalized OZ model. The C2 ... C7 denote different quaternary ammonium cations (blue circles) with respect to the number of side chains' carbon atoms, i.e. 2 ... 7. For comparison, sodium tetraphenylborate (red triangles) is shown. Figure taken from paper **III**.

The data are in quantitative agreement with the prediction based on cation-to-anion size difference as key ingredient [29].

4.4 Paper IV

In situ small-angle x-ray scattering characterization of x-ray induced local heating

As an additional experimental result included in this thesis work, I demonstrate a simple approach for characterizing the x-ray beam-induced local heating. Here, I used again the

water-2,6-DMP binary solvent close to it's critical temperature in a SAXS experiment (paper **IV**) [73].

The local temperature increase during x-ray exposure of a liquid sample in the glass capillary has not been quantified before. We performed measurements at several different temperatures below the mixture's T_C and monitored the temperature both during and in absence of x-ray exposure (T_{nom}). Due to the fact that bulk correlation length ξ follows the 3D Ising universality class in binary liquid mixtures [15, 36], we could determine the temperature increase based on the apparent shift of the divergence of ξ, as exemplified in Fig. 4.4. For the critical water-2,6-DMP solvent, the x-ray induced local temperature was found to be $T_{x-ray} = 0.45 \pm 0.10$ K.

This study demonstrates the application of the binary mixture for characterizing the local heating up of the liquid sample caused by x-ray beam.

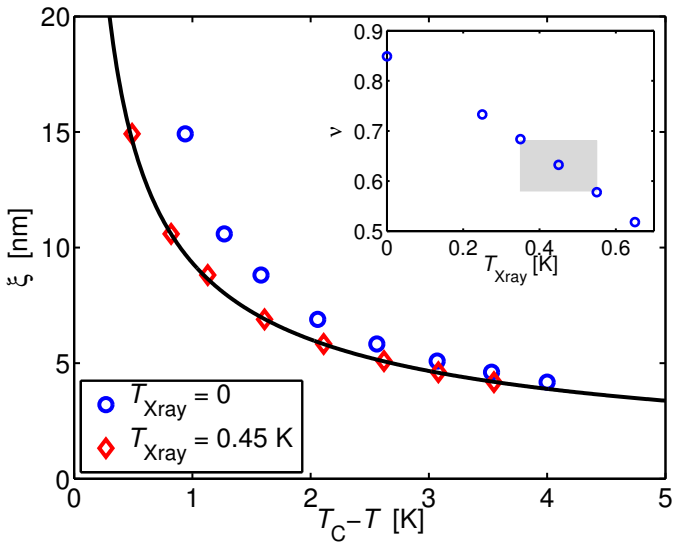

Figure 4.4: Correlation length ξ plotted versus the temperature, where $T = T_{x-ray} + T_{nom}$. The black solid line shows the theoretical prediction $\xi = \xi_0|(T_C - T)/T_C|^{-\nu}$, with $\xi_0 = 0.25$ nm and $\nu = 0.63$. Inset: obtained critical exponent plotted as a function of x-ray induced local temperature increase T_{x-ray}. The $T_{x-ray} = 0.45 \pm 0.10$ K is demonstrated by the gray area. Figure taken from paper **IV**.

5 Conclusions and future outlook

In conclusion, I studied a binary aqueous solvent composed of water and 2,6-dimethylpyridine with focus on ion solvation effects upon addition of hydrophilic and antagonistic type of salt. I used advanced synchrotron-based experimental techniques. In addition, I contributed to the development of the techniques.

This research project could have interesting continuation. First, I see a need for thermodynamic measurements of solubility, following Ref. 23. It would be of high importance to determine the free energy of transfer of ions from water to 2,6-dimethylpyridine, at least for the ions used in this thesis work. This could be then extended to larger amount of different ions. Second, the SAXS investigation in paper **III** can be extended by more measurements of the systems containing quaternary ammonium salts at higher concentrations. Data at higher concentrations would provide information about the eventual more pronounced weak assembly effects in C7. I would find it fascinating to conduct more phase diagram verifications, majority with quaternary ammonium compounds. These would be used in order to find out if e.g. larger concentrations can change the phase behavior or test some compounds with longer carbon chains. Lastly, I would be interested in obtaining deeper understanding of the turbid C7 sample at low 2,6-dimethylpyridine composition. The observed sample's behavior, becoming milky directly after mixing all chemicals, is in line with similar reports in literature [74]. This phenomenon is related to the so-called Ouzo effect associated with spontaneous emulsification in ternary mixtures [75] and nano-structuring has been found near the coexistence line. The latter is referred to as a pre-Ouzo effect [76]. This pre-Ouzo effect together with weak assembly are highly important in designing surfactant-free microemulsions [77, 78].

I believe that the above proposed ideas could contribute to better understanding of binary liquid systems containing salts.

Bibliography

[1] V. Valmacco, M. Elzbieciak-Wodka, D. Herman, G. Trefalt, P. Maroni, and M. Borkovec, "Forces between silica particles in the presence of multivalent cations," *J. Colloid and Interface Sci.*, vol. 472, pp. 108–115, 2016.

[2] S. Ghosal, J. C. Hemminger, H. Bluhm, B. S. Mun, E. L. D. Hebenstreit, G. Kettler, D. F. Ogletree, F. G. Roquejo, and M. Salmeron, "Electron spectroscopy of aqueous solution interfaces reveals surface enhancement of halides," *Science*, vol. 307, pp. 563–566, 2005.

[3] P. Jungwirth and D. J. Tobias, "Specific ion effects at the air/water interface," *Chem. Rev.*, vol. 106, pp. 1259–1281, 2006.

[4] V. Padmanabhan, J. Daillant, L. Belloni, S. Mora, M. Alba, and O. Konovalov, "Specific ion adsorption and short-range interactions at the air aqueous solution interface," *Phys. Rev. Lett.*, vol. 99, p. 086105, 2007.

[5] G. Luo, S. Malkova, J. Yoon, D. G. Schultz, B. Lin, M. Meron, I. Benjamin, P. Vanysek, and M. Schlossman, "Ion distributions near a liquid-liquid interface," *Science*, vol. 311, pp. 216–218, 2006.

[6] U. Nellen, J. Dietrich, L. Helden, S. Chodankar, K. Nygård, J. F. van der Veen, and C. Bechinger, "Salt-induced changes of colloidal interactions in critical mixtures," *Soft Matter*, vol. 7, pp. 5360–5364, 2011.

[7] V. D. Nguyen, M. T. Dang, T. A. Nguyen, and P. Schall, "Critical Casimir forces for colloidal assembly," *J. Phys.: Condens. Matter*, vol. 28, p. 043001, 2016.

[8] K. Sadakane, A. Onuki, K. Nishida, S. Koizumi, and H. Seto, "Multilamellar structures induced by hydrophilic and hydrophobic ions added to a binary mixture of D_2O and 3-methylpyridine," *Phys. Rev. Lett.*, vol. 103, p. 167803, 2009.

[9] A. Onuki, S. Yabunaka, T. Araki, and R. Okamoto, "Structure formation due to antagonistic salts," *Curr. Opin. Colloid Interface Sci.*, vol. 22, pp. 59–64, 2016.

[10] S. Samin, M. Hod, E. Melamed, M. Gottlieb, and Y. Tsori, "Experimental demonstration of the stabilization of colloids by addition of salt," *Phys. Rev. Applied*, vol. 2, p. 024008, 2014.

[11] M. Fukuto, Y. F. Yano, and P. S. Pershan, "Critical Casimir effect in three-dimensional Ising systems: Measurements on binary wetting films," *Phys. Rev. Lett.*, vol. 94, p. 135702, 2005.

[12] C. Gögelein, M. Brinkmann, M. Schröter, and S. Herminghaus, "Controlling the formation of capillary bridges in binary liquid mixture," *Langmuir*, vol. 26, pp. 17184–17189, 2010.

[13] C. Hertlein, L. Helden, A. Gambassi, S. Dietrich, and C. Bechinger, "Direct measurement of critical Casimir forces," *Nature*, vol. 451, pp. 172–175, 2008.

[14] P. D. Gallagher, M. L. Kurnaz, and J. V. Maher, "Aggregation in polystyrene-sphere suspensions in near-critical binary liquid mixtures," *Phys. Rev. A*, vol. 46, pp. 7750–7755, 1992.

[15] M. Krech, *The Casimir effect in critical systems*. Singapore: World Scientific, 1 ed., 1994.

[16] X. Lu, S. G. J. Mochrie, S. Narayanan, A. R. Sandy, and M. Sprung, "Temperature-dependent structural arrest of silica colloids in a water-lutidine binary mixture," *Soft Matter*, vol. 6, pp. 6160–6177, 2010.

[17] V. D. Nguyen, S. Faber, Z. Hu, G. H. Wegdam, and P. Schall, "Controlling colloidal phase transitions with critical Casimir forces," *Nat. Commun.*, vol. 4, p. 1584, 2011.

[18] P. B. Shelke, V. D. Nguyen, A. V. Limaye, and P. Schall, "Controlling colloidal morphologies by Critical Casimir Forces," *Adv. Mater.*, vol. 25, pp. 1499–1503, 2013.

[19] R. Okamoto and A. Onuki, "Charged colloids in an aqueous mixture with a salt," *Phys. Rev. E*, vol. 84, p. 051401, 2011.

[20] M. Bier, A. Gambassi, and S. Dietrich, "Local theory for ions in binary liquid mixtures," *J. Chem. Phys.*, vol. 137, p. 034504, 2012.

[21] S. Samin and Y. Tsori, "The interaction between colloids in polar mixtures above T_C," *J. Chem. Phys.*, vol. 136, p. 154908, 2012.

[22] F. Pousaneh, A. Ciach, and A. Maciołek, "How ions in solution can change the sign of the critical Casimir potential," *Soft Matter*, vol. 10, pp. 470–483, 2014.

[23] H. D. Inerowicz, W. Li, and I. Persson, "Determination of the transfer thermodynamic functions for some monovalent ions from water to N,N-dimethylthioformamide, and for some anions from water to methanol, dimethyl sulfoxide, acetonitrile and pyridine, and standard electrode potentials of some $M^+/M(s)$ couples in N,N-dimethylthioformamide," *J. Chem. Soc. Faraday Trans.*, vol. 90, pp. 2223–2234, 1994.

[24] J. Leys, D. Subramanian, E. Rodezno, B. Hammouda, and M. A. Anisimov, "Mesoscale phenomena in solutions of 3-methylpyridine, heavy water, and an antagonistic salt," *Soft Matter*, vol. 9, pp. 9326–9334, 2013.

[25] K. Sadakane, M. Nagao, H. Endo, and H. Seto, "Membrane formation by preferential solvation of ions in mixture of water, 3-methylpyridine, and sodium tetraphenylborate," *J. Chem. Phys.*, vol. 139, p. 234905, 2013.

[26] K. Sadakane, H. Endo, K. Nishida, and H. Seto, "Lamellar/disorder phase transition in a mixture of water/2,6-dimethylpyridine/antagonistic salt," *J. Solution Chem.*, vol. 43, pp. 1722–1731, 2014.

[27] A. Onuki and H. Kitamura, "Solvation effects in near-critical binary mixtures," *J. Chem. Phys.*, vol. 121, pp. 3143–3151, 2004.

[28] F. Pousaneh and A. Ciach, "The effect of antagonistic salt on a confined near-critical mixture," *Soft Matter*, vol. 10, pp. 8188–8201, 2014.

[29] M. Bier and L. Harnau, "The structure of fluids with impurities," *Z. Phys. Chem.*, vol. 226, pp. 807–814, 2012.

[30] K. Sadakane, Y. Horikawa, M. Nagao, and H. Seto, "The effect of tetraphenylphosphonium choride on phase behavior and nanoscale structures in a mixtures of D_2O and 3-methylpyridine," *Chem. Lett.*, vol. 41, pp. 1075–1077, 2012.

[31] E. Gülari, A. F. Collings, R. L. Schmidt, and C. J. Pings, "Light scattering and shear viscosity studies of the binary system 2,6-lutidine-water in the critical region," *J. Chem. Phys.*, vol. 56, pp. 6169–6179, 1972.

[32] D. Beysens and D. Estéve, "Adsorption phenomena at the surface of silica spheres in a binary liquid mixture," *Phys. Rev. Lett.*, vol. 19, pp. 2123–2126, 1985.

[33] C. A. Grattoni, R. A. Dawe, C. Y. Seah, and J. D. Gray, "Lower critical solution coexistence curve and physical properties (density, viscosity, surface tension, and interfacial tension) of 2,6-lutidine + water," *J. Chem. Eng. Data*, vol. 38, pp. 516–519, 1993.

[34] V. Balevicius and H. Fuess, "Effect of ions on phase diagrams of binary systems," *Phys. Chem. Chem. Phys.*, vol. 1, pp. 1507–1510, 1999.

[35] J. J. Hegseth, A. Oprisan, Y. Garrabos, and D. Beysens, "Imaging critical fluctuations of pure fluids and binary mixtures," *Phys. Rev. E*, vol. 90, p. 022127, 2014.

[36] J. P. Hansen and I. R. McDonald, *Theory of Simple Liquids*. Amsterdam: Academic Press, 3 ed., 2006.

[37] Y. Marcus, "Tetraalkylammonium ions in aqueous and non-aqueous solutions," *J. Solution Chem.*, vol. 37, pp. 1071–1098, 2008.

[38] C. Y. Seah, C. A. Grattoni, and R. A. Dawe, "The effect of halides on the lower critical solution temperature of the 2,6-lutidine-water system," *Fluid Phase Equilibr.*, vol. 89, pp. 345–350, 1993.

[39] K. Sadakane, N. Iguchi, M. Nagao, H. Endo, Y. B. Melnichenko, and H. Seto, "2D-Ising-like critical behavior in mixtures of water and 3-methylpyridine including antagonistic salt or ionic surfactant," *Soft Matter*, vol. 7, pp. 1334–1340, 2011.

[40] K. Aoki, M. Li, J. Chen, and T. Nishiumi, "Spontaneous emulsification at oil-water interface by tetraalkylammonium chloride," *Electrochem. Commun.*, vol. 11, pp. 239–241, 2009.

[41] K. Tamaki, "The surface activity of tetra-n-alkylammonium halides in aqueous solutions. The effect of hydrophobic hydratation," *Bull. Chem. Soc. Jpn.*, vol. 47, p. 2764, 1974.

[42] K. Dopierala and K. Prochaska, "The effect of molecular structure on the surface properties of selected quaternary ammonium salts," *J. Colloid Interface Sci.*, vol. 321, pp. 220–226, 2008.

[43] S. Lindenbaum and G. E. Boyd, "Osmotic and activity coefficients for the symmetrical tetraalkyl ammonium halides in aqueous solution at 25°," *J. Phys. Chem.*, vol. 68, pp. 911–917, 1964.

[44] J. Als-Nielsen and D. McMorrow, *Elements of modern x-ray physics*. Chichester: John Wiley & Sons, Ltd., 2 ed., 2011.

[45] P. Willmott, *An introduction to synchrotron radiation: Techniques and applications*. Chichester: John Wiley & Sons, Ltd., 1 ed., 2011.

[46] J. Daillant and A. Gibaud, *X-ray and neutron reflectivity: Principles and applications*. Berlin Heidelberg: Springer-Verlag, 1 ed., 2009.

[47] M. J. Bedzyk, G. M. Bommarito, and J. S. Schildkraut, "X-ray standing waves at a reflecting mirror surface," *Phys. Rev. Lett.*, vol. 62, pp. 1376–1379, 1989.

[48] W. B. Yun and J. M. Bloch, "X-ray near total external fluorescence method: Experiment and analysis," *J. Appl. Phys.*, vol. 68, pp. 1421–1428, 1990.

[49] N. N. Novikova, E. A. Yurieva, S. I. Zheludeva, M. V. Kovalchuk, N. D. Stepina, A. L. Tolstikhina, R. V. Gaynutdinov, D. V. Urusova, T. A. Matkovskaya, A. M. Rubtsov, O. D. Lopina, A. I. Erko, and O. V. Konovalov, "X-ray fluorescence methods for investigations of lipid/protein membrane models," *J. Synchrotron. Rad.*, vol. 12, pp. 511–516, 2005.

[50] E. Schneck and B. Demé, "Structural characterization of soft interfaces by standing-wave fluorescence with x-rays and neutrons," *Curr. Opin. Colloid Interface Sci.*, vol. 20, pp. 244–252, 2015.

[51] A. Korytowski, W. Abuillan, A. Makky, O. Konovalov, and M. Tanaka, "Impact of lipid oxidation on vertical structures and electrostatics of phospholipid monolayers revealed by combination of specular x-ray reflectivity and grazing-incidence x-ray fluorescence," *J. Phys. Chem. B*, vol. 119, pp. 9787–9794, 2015.

[52] E. Schneck, T. Schubert, O. V. Konovalov, B. E. Quinn, T. Gutsmann, K. Brandenburg, R. G. Oliveira, D. A. Pink, and M. Tanaka *Proc. Natl. Acad. Sci. U.S.A.*, vol. 107, pp. 9147–9151, 2010.

[53] "X-ray data booklet." `http://cxro.lbl.gov/x-ray-data-booklet`. Accessed: 2016-04-05.

[54] K. Ohta and H. Ishida, "Matrix formalism for calculation of electric field intensity of light in stratified multilayered films," *Appl. Opt.*, vol. 29, pp. 1952–1959, 1990.

[55] I. Orlic, K. K. Loh, C. H. Sow, S. M. Tang, and P. Thong, "Parametrization of the total photon mass attenuation coefficients in the energy range $0.1 - 1000$ keV," *Nucl. Instr. Meth. Phys. Res. B*, vol. 74, pp. 352–361, 1993.

[56] B. L. Henke, E. M. Gullikson, and J. C. Davis, "X-ray interactions: Photoabsorption, scattering, transmission, and reflection at $e = 50 - 30,000$ eV, $z = 1 - 92$," *At. Data Nucl. Data Tables*, vol. 54, pp. 181–342, 1993.

[57] L. Parratt, "Surface studies of solids by total reflection of x-rays," *Phys. Rev.*, vol. 95, pp. 309–369, 1954.

[58] D.-M. Smilgies, N. Boudet, B. Struth, and O. Konovalov, "Troika II: a versatile beamline for the study of liquid and solid interfaces," *J. Synchrotron. Rad.*, vol. 12, pp. 329–339, 2005.

[59] "ID10 - Soft interfaces and coherent scattering beamline." `http://www.esrf.eu/UsersAndScience/Experiments/CBS/ID10`. Accessed: 2016-04-03.

[60] L. Feng, S. Barkan, J. S. Iwanczyk, B. E. Patt, and C. R. Tull, "Vortex - a new high performance silicon multi-cathode detector for XRD and XRF applications." `http://www.aps.anl.gov/Xray_Science_Division/Detectors/Detector_Pool/Detector_Information/Vortex_SDD_SII_Nano/Vortex_Theory/docs/Vortex_Paper.pdf`. Accessed: 2016-04-20.

[61] O. Glatter and O. Kratky, *Small Angle X-ray Scattering*. London: Academic Press, 1 ed., 1982.

[62] P. Lindner and T. Zemb, *Neutrons, x-rays and light: Scattering methods applied to soft condensed matter*. Amsterdam: Elsevier, 1 ed., 2002.

[63] "cSAXS - X12SA: Coherent small-angle x-ray scattering." `https://www.psi.ch/sls/csaxs/`. Accessed: 2016-04-03.

[64] B. Henrich, A. Bergamaschi, C. Broennimann, R. Dinapoli, E. F. Eikenberry, I. Johnson, M. Kobas, P. Kraft, A. Mozzanica, and B. Schmitt, "The PILATUS: A single photon counting pixel detector for x-ray applications," *Nucl. Instr. and Meth. Phys. Res. A*, vol. 607, pp. 247–249, 2009.

[65] A. Labrador, Y. Cerenius, C. Svensson, K. Theodor, and T. Plivelic, "The yellow mini-hutch for SAXS experiments at MAX IV laboratory," *J. Phys.: Conf. Ser.*, vol. 425, p. 072019, 2012.

[66] C. Broennimann, E. F. Eikenberry, B. Henrich, R. Horisberger, G. Huelsen, E. Pohl, B. Schmitt, C. Schulze-Briese, M. Suzuki, T. Tomizaki, H. Toyokawa, and A. Wagner, "The PILATUS 1M detector," *J. Synchrotron Rad.*, vol. 13, pp. 120–130, 2006.

[67] M. Witala, R. Nervo, O. Konovalov, and K. Nygård, "Microscopic segregation of hydrophilic ions in critical binary aqueous solvents," *Soft Matter*, vol. 11, pp. 5883–5888, 2015.

[68] J. H. J. Cho, B. M. Law, and K. Gray, "Strong critical adsorption at the liquid-vapor surface of a nonpolar mixture," *J. Chem. Phys.*, vol. 116, pp. 3058–3062, 2002.

[69] M. D. Brown, B. M. Law, L. Marchand, L. B. Lurio, I. Kuzmenko, T. Gog, and W. A. Hamilton, "X-ray and ellipsometric study of strong critical adsorption," *Phys. Rev. E*, vol. 75, p. 061606, 2007.

[70] M. E. Leniussen, C. G. Christova, A.-P. Hynninen, C. P. Royall, A. I. Campbell, A. Imhof, M. Dijkstra, R. van Roij, and A. van Blaaderen, "Ionic colloidal crystals of oppositely charged particles," *Nature*, vol. 437, pp. 235–240, 2005.

[71] M. Witala and K. Nygård, "Relative adsorption excess of ions in binary solvents determined by grazing-incidence x-ray fluorescence," *Manuscript*, 2016.

[72] M. Witala, S. Lages, and K. Nygård, "Mesoscale ordering in binary aqueous solvents induced by ion size asymmetry," *Soft Matter*, 2016. In press, DOI: 10.1039/C6SM00580B.

[73] M. Witala, J. Han, A. Menzel, and K. Nygård, "In situ small-angle x-ray scattering characterization of x-ray induced local heating," *J. Appl. Cryst.*, vol. 47, pp. 2078–2080, 2014.

[74] A. E. Robertson, D. H. Phan, J. E. Macaluso, V. N. Kuryakov, E. V. Jouravleva, C. E. Bertrand, I. K. Yudin, and M. A. Anisimov, "Mesoscale solubilization and critical phenomena in binary and quasi-binary solutions of hydrotropes," *Fluid Phase Equilibr.*, vol. 407, pp. 243–254, 2016.

[75] S. A. Vitale and J. L. Katz, "Liquid droplet dispersions formed by homogeneous liquid-liquid nucleation: "the Ouzo effect"," *Langmuir*, vol. 19, pp. 4105–4110, 2003.

[76] V. Fischer, J. Marcus, D. Touraud, O. Diat, and W. Kunz, "Toward surfactant-free and water-free microemulsions," *J. Colloid and Interface Sci.*, vol. 453, pp. 186–193, 2015.

[77] J. Marcus, D. Touraud, S. Prevost, O. Diat, T. Zemb, and W. Kunz, "Influence of additives on the structure of surfactant-free microemulsions," *Phys. Chem. Chem. Phys.*, vol. 17, pp. 32528–32538, 2015.

[78] T. N. Zemb, M. Klossek, T. Lopian, J. Marcus, S. Schöettl, D. Horinek, S. F. Prevost, D. Touraud, O. Diat, S. Marcelja, and W. Kunz, "How to explain microemulsions formed by solvent mixtures without conventional surfactants," *Proc. Natl. Acad. Sci. U.S.A.*, vol. 113, pp. 4260–4265, 2016.

Acknowledgements

First, I would like to thank my supervisor, **Kim Nygård**, for giving me the opportunity to be part and take over this research project. I am grateful for introducing me to the synchrotron experiments and I appreciate all the time, discussions and feedback. I see this four and half years as a great learning process.

Besides my supervisor, I would like to thank **Elisabet Ahlberg**, for taking the role of my examinator including the yearly progress discussions and support of my chosen courses. I also thank **Johan Bergenholtz** for being the co-supervisor.

I want to acknowledge the beamlines staff for assistance and help during the experiments, at ID10: **Oleg Konovalov** and **Roberto Nervo**; at X12SA: **Jun Han** and **Andreas Menzel** and at I911-4: **Sebastian Lages**.

Moreover, I want to thank to:

Emma Eriksson: friend and former officemate, for the coffee break chats, for being the "Swedish grammar support", for all the discussions about the Swedish culture and for reading the first version of my thesis.

Jeanette Ulama: thanks for making space in your lab for my "smelly" samples. During this short time, we were labmates discussing ternary systems phase behavior. I appreciate your feedback after reading the first version of my thesis.

Karl-Mikael Svensson and **Kristin Jonsson**, officemates: for the pleasant working atmosphere in the office and for the effective co-operation during the teaching labs preparations (KEM011).

The members of **Physical Chemistry group** and **Electrochemistry group**: for the interesting seminars and discussions; for creating a very welcoming and pleasant atmosphere in the group.

A special thanks to my **family**: my parents and sister for constant care and support for any of my ideas and choices.